Rapid aerosol particle growth and increase of cloud condensation nucleus activity by secondary aerosol formation and condensation: A case study for regional air pollution in northeastern China

A. Wiedensohler,[1] Y. F. Cheng,[1] A. Nowak,[1] B. Wehner,[1] P. Achtert,[1] M. Berghof,[1] W. Birmili,[1] Z. J. Wu,[1] M. Hu,[2] T. Zhu,[2] N. Takegawa,[3] K. Kita,[3] Y. Kondo,[3] S. R. Lou,[4,5] A. Hofzumahaus,[4] F. Holland,[4] A. Wahner,[4] S. S. Gunthe,[6] D. Rose,[6] H. Su,[6] and U. Pöschl[6]

Received 31 July 2008; revised 6 January 2009; accepted 4 February 2009; published 28 April 2009.

[1] This study was part of the international field measurement Campaigns of Air Quality Research in Beijing and Surrounding Region 2006 (CAREBeijing-2006). We investigated a new particle formation event in a highly polluted air mass at a regional site south of the megacity Beijing and its impact on the abundance and properties of cloud condensation nuclei (CCN). During the 1-month observation, particle nucleation followed by significant particle growth on a regional scale was observed frequently (~30%), and we chose 23 August 2006 as a representative case study. Secondary aerosol mass was produced continuously, with sulfate, ammonium, and organics as major components. The aerosol mass growth rate was on average 19 μg m^{-3} h^{-1} during the late hours of the day. This growth rate was observed several times during the 1-month intensive measurements. The nucleation mode grew very quickly into the size range of CCN, and the CCN size distribution was dominated by the growing nucleation mode (up to 80% of the total CCN number concentration) and not as usual by the accumulation mode. At water vapor supersaturations of 0.07–0.86%, the CCN number concentrations reached maximum values of 4000–19,000 cm^{-3} only 6–14 h after the nucleation event. During particle formation and growth, the effective hygroscopicity parameter κ increased from about 0.1–0.3 to 0.35–0.5 for particles with diameters of 40–90 nm, but it remained nearly constant at ~0.45 for particles with diameters of ~190 nm. This result is consistent with aerosol chemical composition data, showing a pronounced increase of sulfate.

Citation: Wiedensohler, A., et al. (2009), Rapid aerosol particle growth and increase of cloud condensation nucleus activity by secondary aerosol formation and condensation: A case study for regional air pollution in northeastern China, *J. Geophys. Res.*, *114*, D00G08, doi:10.1029/2008JD010884.

1. Introduction

[2] Northeastern China with the capital Beijing suffers regularly under pollution events with high aerosol mass concentrations. Particle mass concentrations of 200 μg m^{-3} and more are frequently observed especially in the urban area of Beijing [*Wu et al.*, 2008]. There is a great national interest to reduce these high particle mass concentrations.

[3] The city of Beijing and northeastern China are bordered by mountains to the west and north. *Wehner et al.* [2008] analyzed in detail reasons for pollution events in Beijing. The particulate pollution mainly depends on the meteorology situations, on emissions in the city area as well as on point and diffusive sources of particles and precursor gases in the Beijing and neighboring provinces. Depending on mesoscale meteorology, air masses from westerly and northerly directions transport relatively clean continental air to the Beijing area, usually connected with higher wind speeds. This continental air removes possibly existing pollution resulting in relatively low particle mass concentration and clear sky. After this removal, the meteorological conditions often change to slowly moving air masses mainly from southerly or southwesterly directions [*Wehner et al.*, 2008]. Under these conditions, direct particle emissions and

[1]Leibniz Institute for Tropospheric Research, Leipzig, Germany.
[2]State Key Joint Laboratory of Environmental Simulation and Pollution Control, College of Environmental Sciences and Engineering, Peking University, Beijing, China.
[3]RCAST, University of Tokyo, Tokyo, Japan.
[4]ICG-II, Forschungszentrum Jülich, Germany.
[5]Now at School of Environmental Science and Technology, Shanghai Jiaotong University, Shanghai, China.
[6]Biogeochemistry Department, Max Planck Institute for Chemistry, Mainz, Germany.

0148-0227/09/2008JD010884

secondary aerosol formation from precursor gases can lead to an accumulation of particulate mass within the air mass during the following day.

[4] Beside the effects on the regional climate due to elevated light scattering and absorption, high number concentrations of cloud condensation nuclei (CCN) may influence the cloud formation, the microphysics of the cloud, and consequently precipitation in the region of northeastern China. Decreasing trends of the total cloud amount over China has been found in the last 40 years [*Kaiser*, 1998; 2000; *Qian et al.*, 2006]. Central, eastern and northeastern China showed statistically significant decreases of 0.88% and 0.33% per decade in total cloud cover and low cloud cover, respectively [*Qian et al.*, 2006]. The phenomenon of "north drought with south flooding" [*Menon et al.*, 2002] may be caused not only by the purely natural climate change, such as the southward move of the summer monsoon rainy belt in east China, started in the late 1970s to early 1980 [*Xu*, 2001], but also by the acceleration of industrialization in east China emitting large volumes of SO_2 and aerosol particles. High aerosol loading and strong light absorption has been found to have a great climate effect in China modifying the precipitation and surface temperature [*Menon et al.*, 2002]. However, so far there has not been any study about measurements of CCN in China, which could be a base of modeling cloud formation and cloud microphysical properties.

[5] In summer 2006, an international field study, Campaigns of Air Quality Research in Beijing and Surrounding Region 2006 (CAREBeijing-2006), was organized by Peking University to identify the sources of primary and secondary aerosol sources. One of the major goals was to advise the local government on taking actions to reduce local particulate pollution during the Olympic Games. Beside actions to be taken in the city of Beijing such as reduction of car traffic or relocating power and industrial plants, the influence of the regional aerosol on the urban pollution has to be minimized. Previous studies indicated that the regional aerosol may dominate the particle mass concentration in Beijing under certain meteorological conditions [*Streets et al.*, 2007; *Wehner et al.*, 2008].

[6] The Leibniz Institute for Tropospheric Research was involved together with the Peking University, the Research Centre Jülich, the Max Planck Institute Mainz, the University Tokyo, and other Chinese institutes in the CAREBeijing-2006 project characterizing the regional aerosol and their precursors in Yufa, a small town around 50 km in the south of Beijing. This field study was conducted in summer 2006 to study the origin of the regional polluted aerosol under the meteorological conditions expected for the Olympic Games.

[7] In the case study presented here, we investigate the development of physical and chemical aerosol properties. We follow the formation and accumulation of the aerosol by emission of primary aerosol particles as well as secondary nucleation and condensation in a defined air mass within one day. We would like to find out the role of secondary aerosol formation and condensation on the particle growth process, and thus, on the total contribution to the aerosol mass concentration accumulated within a few hours. Combining above mentioned properties with size-resolved CCN measurements allow concluding on the strength of CCN formation in northeastern China during summertime.

2. Experiment

2.1. CAREBeijing-2006 and Yufa Site

[8] As part of the CAREBeijing-2006 campaign, in situ aerosol properties were measured in Yufa (39.51°N, 116.31°E) during the summer of 2006 (12 August to 9 September). Yufa can be defined as a polluted regional site, which is located roughly 50 km south of the urban center of Beijing. A highly trafficked expressway ~1.2 km away passes east of the measurement site. The surroundings of the Yufa site are mainly residential suburban areas.

2.2. Aerosol Inlet System

[9] The measurements have been performed in air-conditioned laboratories at the local university. The aerosol was sampled via a low-flow PM_{10} cyclone inlet (Rupprecht & Patashnick Co., Inc., Thermo, and flow rate 16.67 L min^{-1}) at a height of approximately 25 m and dried by an automated diffusion dryer keeping the relative humidity (RH) below ~30%. The diffusion driers were alternately regenerated with dry compressed air, and the regeneration cycles were about 15 to 50 min depending on the ambient RH.

2.3. Number Size Distribution

[10] Particle number size distributions were measured with an 8-min resolution using a Twin Differential Mobility Particle Sizer (TDMPS) [*Birmili et al.*, 1999] and an Aerodynamic Particle Sizer (APS, TSI 3321). Mobility distributions were inverted to number size distributions using the algorithm of *Stratmann and Wiedensohler* [1996]. Aerodynamic particle sizes measured by the APS have been converted to Stokes diameter using a density of 1.6 g cm^{-3}, estimated on the basis of the analyzed particle chemical compositions [*van Pinxteren et al.*, 2009]. Corrections considering diffusional and gravitational losses in the sampling system have been applied according to *Willeke and Baron* [1993].

2.4. Volatility

[11] A Volatility Tandem Differential Mobility Analyzer (VTDMA) [*Orsini et al.*, 1996; *Philippin et al.*, 2004] was applied to determine the aerosol volatility based on the changes in particle size between 25° and 300°C for selected particle diameters in the range from 30 to 320 nm. At around 300°–350°C, the nonvolatile materials in submicrometer range found in the continental areas are considered to consist mainly of soot [*Burtscher et al.*, 2001; *Frey et al.*, 2008; *Kondo et al.*, 2006; *Rose et al.*, 2006; *Smith and O'Dowd*, 1996; B. Wehner et al., Mixing state of nonvolatile particle fractions and comparison with absorption measurements in the polluted Beijing region, unpublished manuscript, 2008]. Using a VTDMA, nonvolatile particles can be identified, which can be related to fresh or coated soot particles. In general, clearly low and median volatile ranges can be defined (Wehner et al., unpublished manuscript, 2008). In the low volatile range, the particle diameters did not show obvious change or differed only slightly from the initial selected diameter after heated to 300°C. Therefore, particles in the low volatile fraction were con-

sidered as externally mixed soot. Particles in the median volatile fraction consisted of a soot core coated with a volatile shell. Details about the determination of the volume ratio of the completely volatile materials are described by Wehner et al. (unpublished manuscript, 2008).

2.5. Chemical Composition: Inorganic Ions

[12] Measurements of the size-resolved nonrefractory (vaporized at 600°C under vacuum) aerosol chemical composition of the submicrometer particles were made using a quadrupole aerosol mass spectrometer (Q-AMS, Aerodyne) [*Jayne et al.*, 2000], including SO_4^{2-}, NH_4^+, NO_3^-. Cl^-, and particle organic matter (POM) with respective detection limits of 0.1, 0.4, 0.04, 0.02, and 0.4 μg m^{-3} [*Takegawa et al.*, 2009b]. The particle sizing by AMS is based on the vacuum aerodynamic diameter (D_{va}). The diameters measured by the AMS represent dry diameters because the sample air was dried before introduction into the AMS (RH < 44%). The aerodynamic lens of the AMS allows particles transmission efficiencies of ~100% for D_{va} = 50–600 nm, with some transmission for D_{va} > 1 μm, which is roughly similar to the commonly used PM_1 aerodynamic cutoff [*Takegawa et al.*, 2009a, and the references herein]. The particle collection efficiency (CE) was estimated to be 1.0 for the Yufa measurements [*Takegawa et al.*, 2009b]. The time resolution is 10 min.

2.6. Chemical Composition: Elemental and Total Organic Carbon

[13] Total organic carbon (OC) and elemental carbon (EC) of the ambient submicrometer aerosol was measured every 1 h with an EC/OC online analyzer using a thermal optical technique (Sunset Laboratory Inc., Beaverton, OR, USA). The inlet for this instrument was equipped with a PM_1 cyclone sampling the ambient air and activated carbon denuder. Detailed descriptions of the Sunset EC/OC online analyzer have been given elsewhere [*Kondo et al.*, 2006; *Takegawa et al.*, 2009a].

2.7. Chemical Composition: Water-Soluble Organic Carbon

[14] The total water-soluble organic carbon (WSOC) in the submicrometer particles at ambient conditions (PM_1 cyclone inlet) was measured continuously by an online instrument [*Sullivan et al.*, 2004] with a time resolution of 6 min. It measures WSOC with a particle-into-liquid sampler (PILS). The collected liquid is filtered and the dissolved organic carbon is quantified online by a total organic carbon analyzer (TOC, Model 800 Turbo, Boulder, CO). The detection limit is approximately 1 μg C m^{-3} (3σ of baseline noise, σ refers to the standard deviation) [*Kondo et al.*, 2007].

2.8. OH Reactivity

[15] The local atmospheric OH reactivity is defined as the total pseudo first-order rate coefficient for all atmospheric reactions of OH in an air parcel. The OH reactivity can be experimentally determined as the reciprocal of the measured OH lifetime. Here we use a UV-pump high-repetition-rate LIF-probe technique to measure the OH lifetime in ambient air. Sampled air that contains ozone and water vapor is drawn continuously through a laminar flow tube and is exposed to short UV laser pulses (266 nm, 10 ns) from a frequency-quadrupled Nd:Yag laser running at a pulse repetition frequency of 0.5–1 Hz. OH radicals are generated by laser-flash photolysis of ozone. The subsequent chemical OH decay in the sampled air is monitored by time-resolved laser-induced OH fluorescence, using a high-repetition-rate (8.5 kHz) probe laser at 308 nm. The measured OH decay curves are numerically accumulated for more than 50 times to achieve a good signal-to-noise ratio. From the decay curves the OH lifetime is extracted by a numerical fit routine. The new technique can measure OH reactivities between 1 and 100 s^{-1}, which covers conditions from very clean to much polluted air, within 1–3 min of measurement time. The reactivity is determined by an exponential fit to the observed time-resolved LIF signals (decay curve). The real reactivity is determined by the measured reactivity subtracting the zero air reactivity, which is the measured reactivity in pure synthetic air and mostly contributed by diffusion and turbulence. Owing to the instrument characterization, a nonlinear correction is made to the data whose value is larger than 57 s^{-1}. The precision of the data is less than 10% (1σ), but not better than 4% (1σ). The accuracy is given by two error contributions: 7% relative error and 0.3 s^{-1} (1σ).

2.9. Cloud Condensation Nuclei

[16] Cloud condensation nuclei, i.e., aerosol particles that enable the formation of cloud droplets at a given water vapor supersaturation, were measured with a continuous flow CCN counter (CCNC, Droplet Measurement Technologies, Model CCN-2) [*Lance et al.*, 2006; *Roberts and Nenes*, 2005]. In order to measure size-resolved CCN efficiency spectra (CCN activation curves), the CCN counter was coupled to a Differential Mobility Analyzer (DMA, TSI 3071) and to a condensation particle counter (CPC, TSI 3762) measuring the total number of size-selected aerosol particles (condensation nuclei, CN) [*Frank et al.*, 2006; *Rose et al.*, 2008a].

[17] The effective water vapor supersaturation (S) in the CCN counter was alternately set to 0.07%, 0.26%, 0.46%, 0.66%, and 0.86%, with a relative uncertainty of ~10% (~30% at S = 0.07%). It had been calibrated using ammonium sulfate and an activity parameterization Köhler model (AP3) [*Rose et al.*, 2008a] that can be regarded as the most accurate reference available. Note that other frequently used Köhler models and the corresponding calibrations lines would deviate by up to 20% or more, and care has to be taken when comparing the results of different CCN measurement and model studies [*Rose et al.*, 2008a]. The recorded CCN efficiency spectra (CCN/CN versus particle diameter, 20–300 nm) were corrected for multiple charges, the DMA transfer function, and different counting efficiencies of the CCNC and the CPC [*Frank et al.*, 2006; *Rose et al.*, 2008a]. CCN size distributions were calculated by multiplication of the CCN efficiency spectra with the total aerosol particle number size distributions measured in parallel by the TDMPS. CCN number concentrations were calculated by integrating the CCN size distributions. Effective particle hygroscopicity parameters (κ) were calculated according to equation (6) of *Petters and Kreidenweis* [2007] from the midpoint activation diameters of the measured CCN efficiency spectra, i.e., from the diameters at which

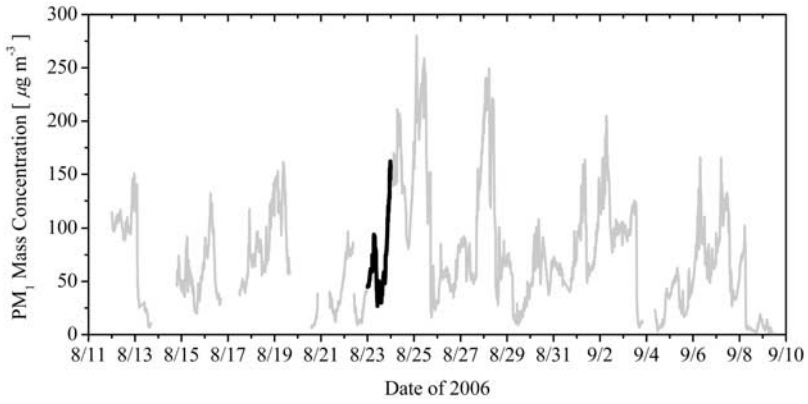

Figure 1. Time series of the PM_1 particle mass concentration determined from number size distribution measurements for the entire CAREBeijing-2006 field study. The black line indicates the time of our case study on 23 August 2006.

CCN/CN reaches half its maximum. For details see *Rose et al.* [2008b].

2.10. Gas Phase and Meteorology Measurements

[18] Measurements of mixing ratios of gas-phase species and meteorological parameters were took place at the Yufa site too, at a height of approximately 20 m.

[19] CO concentration was measured by an NDIR gas analyzer (Thermo Electron Inc., Model 48C, USA) with an integration time of 1 min [*Kondo et al.*, 2006]. SO_2 concentration was monitored by an SO_2 analyzer (Ecotech, ML9850B) with a time resolution of 1 min.

[20] The meteorological parameters, including ambient air temperature (T) and pressure (P), relative humidity (RH), and wind speed and direction (WS and WD) have been measured concurrently with Platinum RTD temperature sensor (YOUNG, 41372C), barometric pressure sensor (YOUNG, 61202V), Vaisala intercap relative humidity sensor (YOUNG, 41372C), and wind monitor (YOUNG, 05103V). The time resolution is 1 min.

3. Observations and Discussion

3.1. New Particle Formation and Rapid Particle Growth

[21] As described above, northeastern China is bordered by mountains to the west and north. Here, the mesoscale meteorology plays an important role [*Wehner et al.*, 2008]. Air masses from westerly and northerly directions transport continental air to the Beijing area. These air masses contain generally less pollution and are connected with higher wind speeds minimizing the accumulation of pollutants. These continental air masses remove the possibly existing pollution resulting in relatively low particle mass concentration and clear sky. Afterward, the meteorological conditions often change to slowly moving air masses mainly from southerly or southwesterly directions resulting in an accumulation of pollutants and subsequently in high particle mass concentrations coupled with low visibilities [*Garland et al.*, 2009].

[22] During the CAREBeijing-2006 study we observed several of these "cycles," which are typical for these region. A time series of the calculated PM_1 particle mass concentration is shown in Figure 1. Here the PM_1 particle mass concentrations were determined with the particle number size distributions measured by TDMPS, using the estimated density of 1.6 g cm^{-3}. One can clearly see cycles of few days in which the mass concentration of the aerosol builds up until the pollution is removed again. In the following, we focus only on the 23 August 2006, which is a representative day for particle formation followed by accumulation of pollutants due to slow winds from the South (marked as black line in Figure 1).

[23] To understand the evolution of the number size distributions on 23 August 2006, they will be discussed together with meteorological parameters (see Figures 2a–2c). On 23 August 2006, the sunrise and sunset occurred at around 0537 and 1904 local time (LT) and the noontide is at about 1221 LT (http://www.pdweather.com/pro/richu.html). Owing to a rapid decrease in particle number and mass concentration, homogenous particle nucleation (Figure 2a) started in the morning after 1000 LT. It is worth to noticing that the particle formation from gas phase and the growth of cluster might start with smaller size, for example 1–2 nm. However, the TDMPS used at the Yufa site was only capable to measure the particles with size down to the 3 nm. Therefore, we defined the particle growth event on 23 August 2006 started at 1000 LT, when it was first "observed" for particles larger than 3 nm. Along with the breakup of the nocturnal inversion layer and developing of daytime boundary layer due to solar heating, we observed significant changes in the wind speed and direction as well as the relative humidity between 0800 and 1000 LT (pick-up of the wind speed to approximately 2 m s^{-1}; see Figure 2c). Subsequently, cleaner air was mixed with the near-ground, more polluted air left from the previous day. The wind direction stabilized to southwesterly directions and the relative humidity dropped significantly. The new particle formation was followed by condensational growth within the slowly moving air mass indicated by the "banana-shaped" temporal development of the number size distribution (see Figure 2a).

[24] In Figure 2b, we evaluated the evolutions of the calculated PM_1 mass concentration and the particle mean diameter, which was derived by mode fitting [*Wu et al.*, 2007]. A nearly linear increase in the particle mean diameter

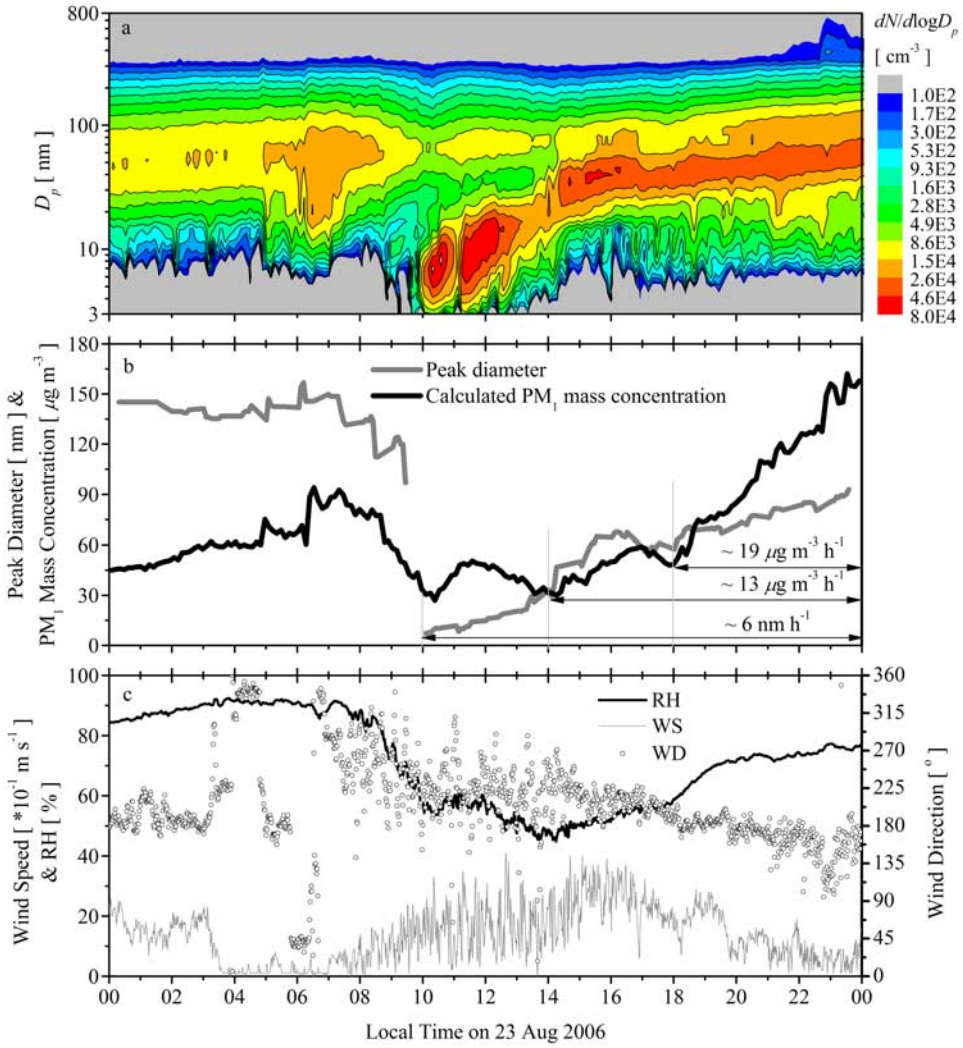

Figure 2. (a) Temporal evolution of the number size distribution at Yufa on 23 August 2006 showing new particle formation and subsequent growth. (b) Temporal evolutions of the PM_1 mass concentration derived from TDMPS number size distributions and peak diameters from mode fitting to the measured size distributions. Average growth rates of the number mode diameter and of the PM_1 mass are indicated. (c) Temporal evolutions of the meteorology parameters, including relative humidity (RH) and wind speed and direction (WS and WD).

emphasized the particle growth from around 1000 LT to the midnight. During about 14 h, the particle mean diameter increased from around 10 nm to approximately 95 nm with a growth rate of ~6 nm h^{-1}. Concurrently, as mentioned above, the PM_1 mass concentration rapidly increased since 1400 LT after the air mass breakup, and the average growth rate was as high as ~13 μg m^{-3} h^{-1}. By investigating the growth of the mass concentration after 1800 LT, the growth rate increased even to ~19 μg m^{-3} h^{-1}. This observation was coupled nicely by the increase in OH reactivity, as we will discuss later.

3.2. Air Mass Identification

[25] Owing to the breakup of the nocturnal inversion, the air mass changed its characteristics. In order to segregate possible physical effects such as evolution of boundary layer and transportation, we normalized certain concentrations of gas-phase and aerosol compounds to mass concentration of EC [*Su et al.*, 2008]. As illustrated in Figure 3a, the ratio of CO to EC, which both primarily originated from the combustion sources kept almost constant from 1000 to 2200 LT. This implies that the scaling method is satisfying in respect to segregating the possible physical effects. However, one could also see that before and after the air mass changing, the ratios of CO to EC were dramatically changed as well, indicating two different air masses. This air mass changing can be also clearly seen in the ratios of Cl^- to EC (see Figure 3b). As shown in Figure 3c, the daytime variation of SO_2 was stronger than those during nighttime. This finding implies (1) that the mixing of SO_2 within the boundary layer is not homogeneous (it might be that SO_2 with higher concentration from elevated layers was mixed with surface air during the boundary layer development) and (2) that EC emissions derive from other sources than the major SO_2 emitters such as coal-fired power plants. Even though SO_2 and EC may come from several common

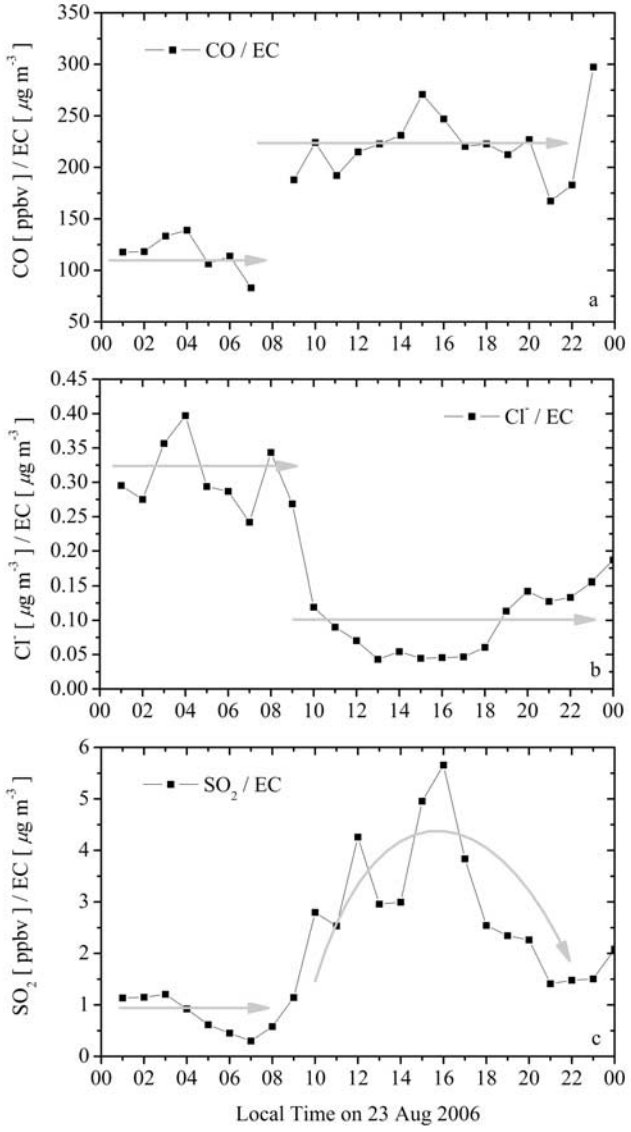

Figure 3. Time series of (a) CO, (b) Cl^-, and (c) SO_2 scaled by EC concentration, as indicators of air mass change. Light gray arrows illustrate the possible changes in the air masses.

sources with different relative amounts, the ratio could be changed owing to chemical transformation.

3.3. Mass Concentration and Chemical Composition

[26] Physically and chemically determined PM_1 particle mass concentrations are shown in Figure 4. The thick solid black line in Figure 4a represents here the calculated mass from TDMPS measurements, as also shown in Figure 2b. Light gray hollow circles are the averaged PM_1 mass according to the time resolution of EC/OC online measurement, which is approximately 1 h. The error bar is derived by varying the particle density from 1.4 to 1.8 $\mu g\ m^{-3}$. The triangles represent the summation of POM, EC, SO_4^{2-}, NH_4^+, NO_3^- and Cl^- determined by chemical analyses. The error bar of ± 10% (1σ) is derived by a simple Monte Carlo simulation (10000 trials) based on the average mass contributions of different compounds and their measurement uncertainties. The uncertainty of POM measured by AMS is conservatively estimated as ± 25% (3σ) [*Kondo et al.*, 2007; *Takegawa et al.*, 2005]. The uncertainty of EC determined by OC/EC online measurements is estimated to be ± (6–10)% (3σ) [*Kondo et al.*, 2006, 2007]. The uncertainties of inorganic ions measured by AMS were about ± 18% (3σ) at the Yufa site [*Takegawa et al.*, 2009b]. However, the AMS in general could have much larger uncertainties up to a factor of 2 as a standalone instrument, mostly due to the uncertainty in CE [*Takegawa et al.*, 2009a].

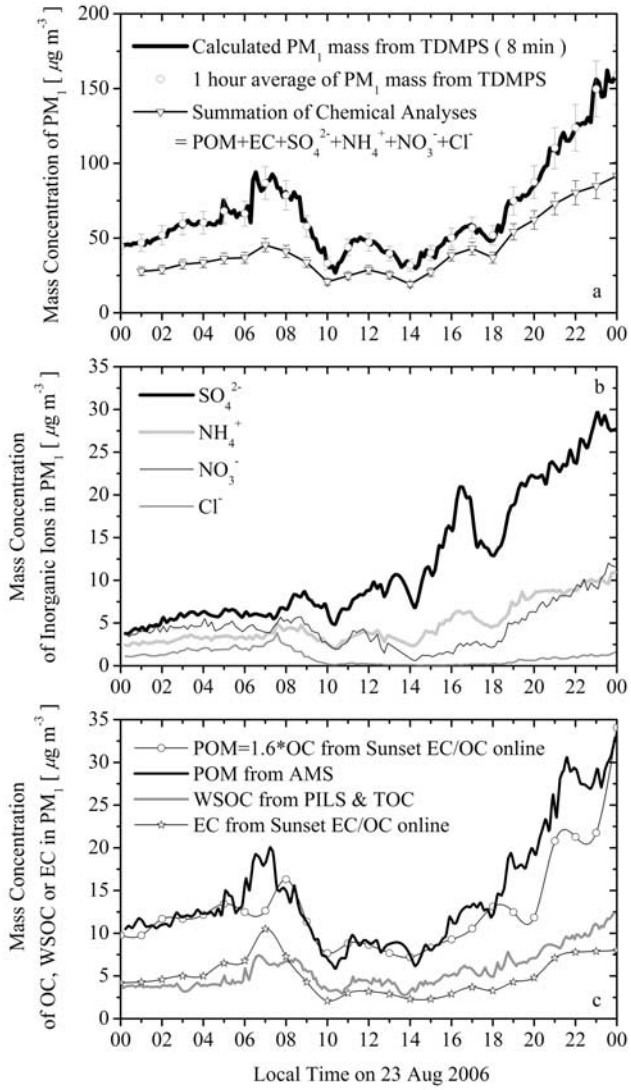

Figure 4. Time series of (a) the PM_1 mass concentrations determined by TDMPS and the summation of major aerosol chemical compositions analyzed by AMS and EC/OC online measurements (error bars represent uncertainties in particle density and chemical analyses, respectively), (b) the mass concentrations of water-soluble inorganic ions (SO_4^{2-}, NH_4^+, NO_3^-, and Cl^-) determined by AMS, and (c) PM_1 mass concentrations for EC, POM (OC of Sunset multiplied with a factor of 1.6) determined by sunset EC/OC online measurements, and WSOC determined by the combined method of PILS and total organic carbon analyzer (TOC).

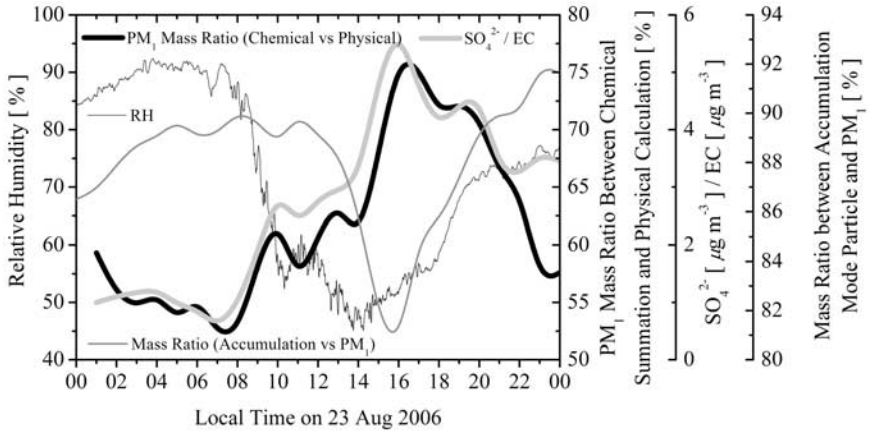

Figure 5. Time series of relative humidity (RH), scaled concentration of SO_4^{2-} by EC, PM_1 mass ratio between the chemical summation and physical calculation from TDMPS, and the mass ratio between accumulation mode particles and total PM_1.

[27] As one can see from Figure 4a, the deviation between the physically and chemically determined PM_1 mass concentrations is rather significant. Note that there is difference between the definitions of the physically and chemically determined PM_1 aerosol. The calculated PM_1 mass concentration from the TDMPS measurements integrated the masses of particles with mobility diameter less than 1 μm at dry conditions (RH < 30%). But AMS provided the concentrations of most aerosol chemical compounds within a vacuum aerodynamic diameter size range from about 50 to 600 nm, whereas in the EC/OC online measurements, the particles were sampled at ambient conditions (RH $\sim$ 40 to 90%) with aerosol dynamic diameter less than 1 μm. *Achtert et al.* [2009] indicated that at Yufa site, when relative humidities were higher than 60–70% the particles showed a significant growth with growth factors of 1.2–1.3 (RH 70%) to 1.4–1.6 (RH 90%), while externally mixed EC was supposed to be hydrophobic. Therefore, it was possible that for the aerodynamic based sampling technique (OC/EC online and the WSOC measurements), few particle matters, especially the water-soluble particle compounds, were sampled at ambient conditions compared with dry conditions. As one can see from Figure 5, during late evening and early morning, the relative humidities were relatively high at about 70–90%, and the PM_1 mass discrepancy between the chemical summation and physical calculation was also relatively large.

[28] Regarding to the sampling of AMS, the approximate of the AMS vacuum aerodynamic size cut to classical PM_1 (aerodynamic) is generally applicable only when the density/shape factor of accumulation mode particle is close unity [*Takegawa et al.*, 2005, and the references herein]. However, the vacuum aerodynamic diameter of certain particle is normally larger than its aerodynamic diameter. This means that AMS actually sampled even less particles than the aerodynamic PM_1. At the same time, the evolution of particle number size distribution (particle growth) might also influence the sampling of AMS [*Takegawa et al.*, 2009b]. Figure 5 presents also the mass ratio between the accumulation mode (150–1000 nm) particles and the total PM_1, calculated from the particle number size distributions by TDMPS. It can be found that when the contribution to PM_1 mass by the accumulation mode particles increased the discrepancy between chemically and physically determined particle masses was also larger. In this situation, a smaller CE might be suggested instead of a constant value 1.0. However, the uncertainty introduced into the mass closure study by this inconsistency of PM_1 definitions is hard to estimate. Another possible reason for the discrepancy is that other chemical compounds have not been analyzed such as mineral dust in the upper accumulation mode, which may account some PM_1 mass fraction, too.

[29] We are rather confident in the number size distribution data measured at approximately 30% RH. An optical closure study for light scattering gave an excellent agreement between calculated (from the number size distribution) and measured light scattering coefficients (correlation coefficient $\geq$ 0.95, discrepancy within ± 8%) [*Cheng et al.*, 2009], which confirmed that the measured particle number size distributions were accurate. Both number size distribution and light scattering coefficient have been measured downstream the same inlet system at the same RH. The mass fraction of water should be however still below 15% at a RH of 30% [*Achtert et al.*, 2009].

[30] In Figures 4b and 4c, we summarized the observations in terms of highly time-resolved chemical composition of the aerosol in the submicrometer range. OC and EC were determined by the Sunset instruments as described before. The concentration of OC was multiplied by a factor of 1.6 to estimate the mass concentration of POM [*Turpin and Lim*, 2001]. While time series of EC (stars), POM (thick black line and open circles), and WSOC (dark gray line) mass concentrations are plotted in Figure 4c, water-soluble inorganic ions (SO_4^{2-}, NH_4^+, NO_3^- and Cl^-) are shown as thick black, light gray, thin black, and dark gray lines, respectively, in Figure 4c. Especially, the mass concentration of major secondary aerosol compounds such as POM, WSOC, SO_4^{2-}, NH_4^+, and NO_3^- increase significantly after 1400 LT which indicates that the particle growth is mainly driven by secondary aerosol formation and condensation. EC increases also continuously, but less pronounced than the secondary aerosol compounds, which will be discussed later.

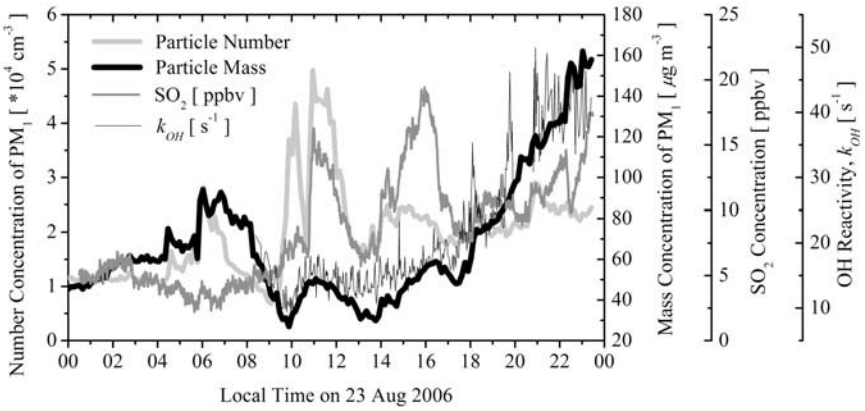

Figure 6. Time series of total particle number, PM_1 mass concentration, SO_2 concentration, and OH reactivity.

3.4. Secondary Aerosol Formation and Condensational Growth

[31] In Figure 6, we compare particle number and mass concentrations with SO_2 as precursor of the major gases and with the OH reactivity. SO_2 emission plumes obviously influenced the particle nucleation and growth. Probably, owing to slight shifts in wind direction or downward mixing, peaks in the SO_2 concentration (dark gray line) appeared from 1000 to 1200 LT and from 1400 to 1700 LT. The evolutions of particle number and mass concentrations (light gray and thick black line) coupled clearly with the peaks in SO_2 concentration (dark gray line). After 1700 LT, the wind direction changed to be more and more toward southerly directions. However, we probably observed still the same regional air mass with our measurements since we followed nicely the ''banana-shaped'' evolution of the number size distribution without further interruptions. While the number concentration only slightly increased, the PM_1 mass concentration (thick black line) increased significantly from around 30–50 $\mu g\ m^{-3}$ at noon to approximately 160 $\mu g\ m^{-3}$ at midnight.

[32] Furthermore, we plotted the OH reactivity as time series in comparison to the PM_1 particle mass concentration. Both, the mass concentration and the OH reactivity, seem to be strongly correlated, which implies that the major fraction of the particle mass is secondary and a product from gas-phase chemical reactions. Note that the OH reactivity is not a measure of the oxidation going on, but the potential oxidation if oxidants are available. Even though, we think the rapid increasing in the particle mass concentration was mainly due to not only the decreasing dilution during nighttime but also the condensational growth of particles, the possible oxidation process in the atmosphere during nighttime is, however, not clear yet.

[33] In order to rule out the physical effect of decreasing dilution during nighttime, we scaled the total PM_1 mass concentration and the major secondary aerosol products such as SO_4^{2-}, NH_4^+, NO_3^-, POM, and WSOC by EC (Figures 7a–7f), respectively, to investigate the role of secondary aerosol formation during particle growth, since EC represents the primary emission.

[34] As shown in Figure 7a, the ratio of PM_1 to EC continuously grew from 0800 LT in the morning until midnight. The increasing PM_1 mass concentration during the nighttime was contributed by both of the decreasing dilution and condensational growth. However, in the present case, increase of the secondary particle mass by condensational growth was very important. First, as one can see from Figures 2a and 2b, the diameters of the nucleation mode and the accumulation mode both increased continuously and significantly. With absent of condensational growth, decreasing dilution cannot lead to this particle diameter growth. On the other hand, we integrated the total particle number concentrations of Aitken mode (60–150 nm) and accumulation mode (150–1000 nm). To rule out the effect of decreasing dilution during the night, we also scaled the integrated particle number concentrations by the EC concentration. As shown in Figure 8, the scaled number concentration of Aitken mode particles reached the highest at around noontime, and decreased rapidly afterward. For the accumulation mode, the scaled particle number concentration increased continuously in the morning and afternoon. However, after 1600 LT, it kept nearly constant or slightly decreased in the late night instead of increasing. The PM_1 mass concentration was dominated by the accumulation mode particles (see Figure 5). Comparing the increasing trend of the scaled PM_1 mass concentration (see Figure 7a), we can conclude that the condensational growth contributed significant mass growth in the submicrometer range during nighttime, which hence proved not only was contributed by the accumulation due to the decreasing dilution and/or emission.

[35] The mass fractions of the secondary aerosol compounds (SO_4^{2-}, NH_4^+, POM, and WSOC) also increase in the late afternoon and early evening (see Figures 7b, 7c, 7e, and 7f). According to measurements, the secondary aerosol formation levels off or slightly decreases against the EC mass concentration in the late night. Only NO_3^- shows a slightly different pattern with a minimum around noontime and continuous growth afterward (see Figure 7d). The different behavior might be caused by the equilibrium of ammonium nitrate and/or nitric acid between the gas and solid phases due to their semivolatile nature. Some of the organics in POM are also semivolatile as nitrate, and they may have higher concentration during the nighttime compared to the daytime.

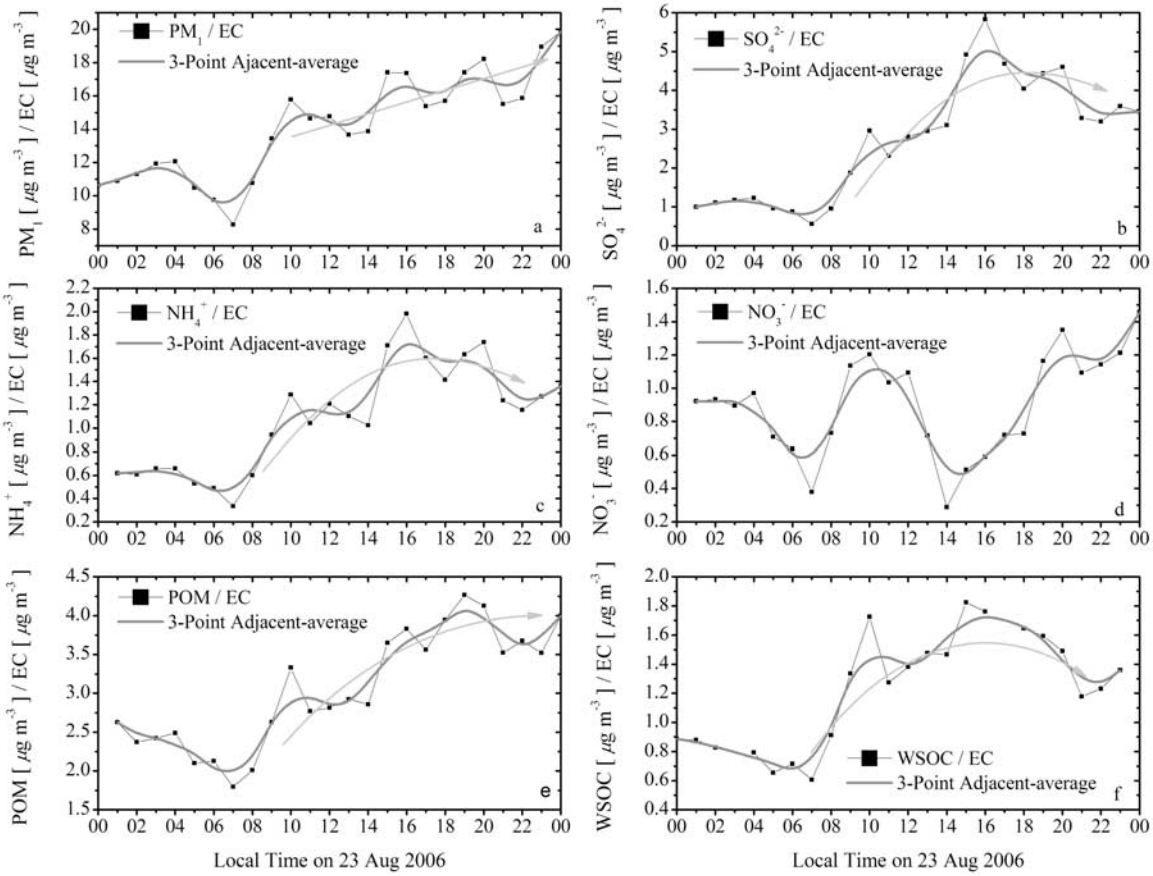

Figure 7. Time series of (a) PM_1 mass concentration derived from TDMPS number size distribution, (b) SO_4^{2-}, (c) NH_4^+, (d) NO_3^-, (e) POM, and (f) WSOC, scaled by EC concentration to indicate the secondary formation. Dark gray lines present the three-point adjacent average. Light gray arrows illustrate trends.

[36] By comparing the scaled mass concentration of SO_4^{2-} by EC with the mass ratio between the chemically and physically determined PM_1 mass concentrations, which showing the discrepancy of these two methods, we found that they followed each other nicely (see Figure 5). Therefore, one possible reason why the scaled PM_1 mass concentration determined from TDMPS increased during the night whereas the scaled concentrations of those important chemically determined secondary particle compounds, such as SO_4^{2-}, NH_4^+, and WSOC, slightly decreased or kept the same concentration level might be the different definitions of the physically and chemically determined PM_1 and the sampling issues of OC/EC online, WSOC, and AMS measurements as already discussed before.

[37] According to the ratio of SO_4^{2-}, NH_4^+, POM, and WSOC to EC (see Figure 7), the sum of (SO_4^{2-}/EC) and (NH_4^+/EC) is nearly twice of the ratio between POM and EC. This may indicate that at the polluted regional site near Beijing in northeastern China, secondary sulfate and POM both significantly contribute to the particle growth. Secondary sulfate may play a more important role, especially during the daytime and heavily polluted periods [*Takegawa et al.*, 2009a].

[38] Another indicator of condensational growth is the mass fraction of volatile aerosol material. In Figure 9, a time series of this mass fraction is plotted for five different particles sizes (100, 150, 200, 260, and 320 nm) investigated by the VTDMA. In the morning after the breakup of the nocturnal inversion layer, the volatile mass fraction drops significantly indicating a stronger influence of non-

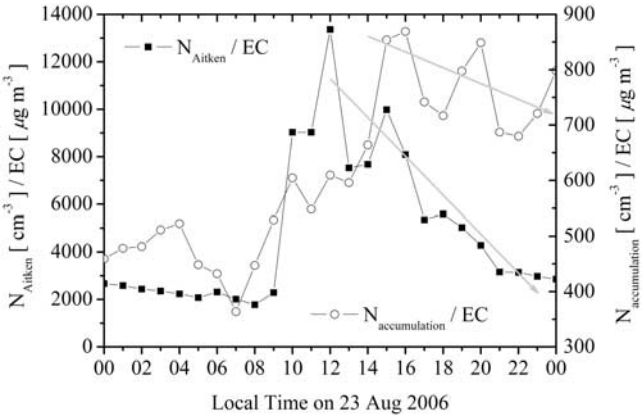

Figure 8. Time series of integrated particle number concentrations of Aitken mode (60–150 nm) and accumulation mode (150–1000 nm), scaled by EC concentration to rule out the effect of decreasing dilution during nighttime. Light gray arrows illustrate trends.

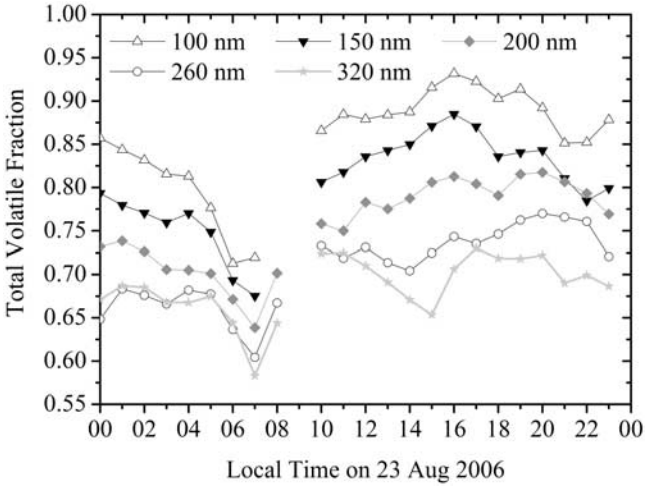

Figure 9. Time series of the size-resolved volatile volume fraction determined from the VTDMA measurements. Here the open triangles, black triangles, gray diamonds, open circles, and gray stars represents 100-, 150-, 200-, 260-, and 320-nm particles, respectively.

volatile particles (probably soot in this size range). Afterward, the volatile mass fraction increases significantly for all particle sizes, however especially for 100 and 150 nm particles, indicating the condensational growth of secondary aerosol material. In the evening, the mass fraction of volatile material slightly decreased again owing to a reduced secondary aerosol formation compared to the direct emission of nonvolatile material such as soot.

[39] We can conclude that secondary aerosol production was the major source for the particle growth of nucleated particle into the size range of possible CCN. Especially, SO_4^{2-}, NH_4^+, and POM contributed to the growth by secondary aerosol production.

3.5. Cloud Condensation Nuclei

[40] Figure 10 illustrates the evolution of the number size distribution of aerosol particles (CN, Figure 10a) and cloud condensation nuclei measured at different water vapor supersaturation levels (CCN, Figures 10b–10d) from the nucleation event in the late morning until the end of the day.

[41] After the nucleation event in the morning (until ~1200 LT), only preexisting accumulation mode particles acted as CCN because the newly formed particles were still too small (open gray squares). The situation changed after midday, when the newly formed particles grew into the CCN size range while the CCN accumulation mode increased in size and number (solid gray squares). These trends continued through the evening (open black circles) and night (solid black circles).

[42] At low supersaturation (S = 0.07%, Figure 10b), the shape of the CCN size distribution with a single mode at ~200 nm remained practically the same throughout the day, while the peak height increased continuously with the growth of the accumulation mode in the particle number size distribution (see Figure 10a).

[43] At medium supersaturation (S = 0.46%, Figure 10c), the CCN size distribution in the morning was nearly

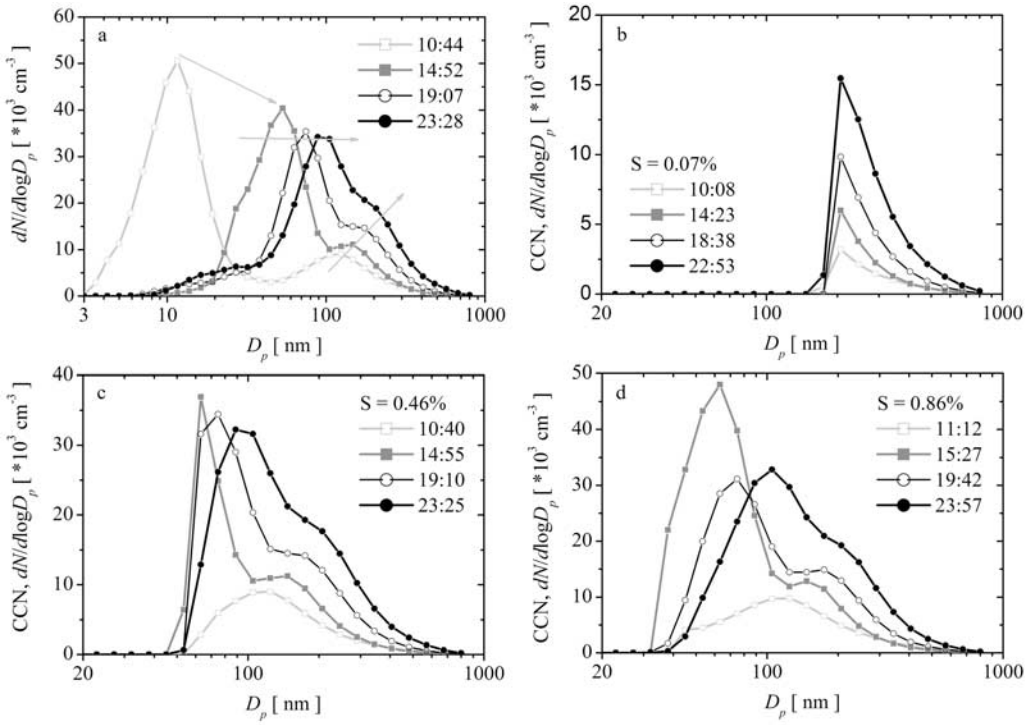

Figure 10. Evolution of (a) the particle number size distribution measured by TDMPS, and CCN number size distributions at selected water vapor supersaturation levels: (b) 0.07%, (c) 0.46%, and (d) 0.86% from about 1000 LT to midnight. Light gray arrows illustrate the diameter growth of different particle modes.

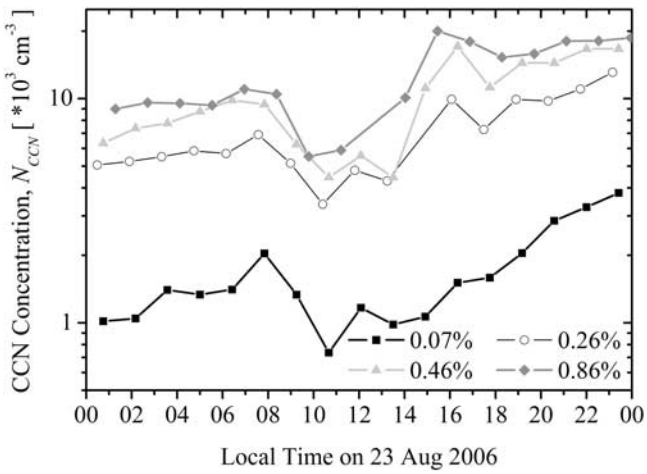

Figure 11. Time series of the total CCN concentration measured from selected supersaturations (0.07%, 0.26%, 0.46%, and 0.86%).

identical to the accumulation mode of the CN size distribution with a mode diameter of 120 nm (see Figure 12d later in this section). In the course of the day, the CCN accumulation mode grew both in height and diameter (up to ~200 nm) and a second CCN mode appeared at smaller diameters (~60–100 nm). The second CCN mode corresponded to the grown nucleation mode of the number size distribution, and the number of CCN in this mode was comparable to the number of CCN in the accumulation mode.

[44] At high supersaturation (S = 0.86%, Figure 10d), the CCN size distribution in the morning was dominated by the number concentration in the accumulation mode, but already exhibited a shoulder at ~45 nm, which corresponded to the right side of the fresh nucleation mode. Throughout the rest of the day, the small CCN mode that corresponded to the growing nucleation mode (~60–100 nm) dominated the CCN size distribution, and the number of CCN in this mode was by a factor of 2–3 larger than in the accumulation mode. To our knowledge, this is the first observation of a CCN size distribution, which is not dominated by the accumulation mode but by a growing nucleation mode. However, this might also be due to the fact that there still are very little data on size-resolved CCN properties.

[45] Figure 11 shows the time series of the integral CCN number concentration (N_{CCN}) at different supersaturations. Owing to the air mass change, N_{CCN} generally decreased in the early morning prior to the nucleation event (by a factor of 2–3 from 0700 to 1000 LT). After the nucleation event, N_{CCN} increased at different rates for different supersaturations.

[46] At low supersaturation (S = 0.07%), N_{CCN} increased exponentially over ~13 h from a minimum value of 700 cm^{-3} up to 4000 cm^{-3}. At medium and high supersaturation (S = 0.26–0.86%), however, N_{CCN} increased very rapidly over ~6 h during the afternoon, and remained nearly constant during the evening (13,000–19,000 cm^{-3}, respectively).

[47] By the end of the day, the relative increase of N_{CCN} at high supersaturation (S = 0.86%, +200% relative to 1000 LT; +100% relative to 0000 LT) was significantly lower than at low supersaturation (S = 0.07%, +400% relative to 1000 LT; +300% relative to 0000 LT). On Jeju Island, Korea, *Kuwata et al.* [2008] measured recently after a nucleation event CCN number concentration up to 7,000 cm^{-3} for a supersaturation of 0.97%. In any case, the CCN concentrations measured at the end of 23 August 2006 were among the highest ever observed [*Andreae*, 2008; *Andreae and Rosenfeld*, 2008]. Higher concentrations were only measured near Guangzhou, China, during the PRIDE-PRD2006 campaign [*Rose et al.*, 2008b]. It seems to be that particle nucleation events are important for the formation of CCN in this region.

[48] Figure 12 shows the time series of the effective hygroscopicity parameter κ as derived from the measured CCN efficiency spectra. κ describes the influence of chemical composition on the CCN activity of aerosol particles, i.e., on their ability to absorb water vapor and act as CCN. It relates the dry diameter of aerosol particles to the so-called critical water vapor supersaturation, i.e., the minimum supersaturation required for cloud droplet formation [*Petters and Kreidenweis*, 2007; *Pöschl et al.*, 2009].

[49] According to measurements and thermodynamic models (Köhler theory), κ is ~0 for insoluble materials like soot, ~0.1 for (secondary) organic aerosols and biomass burning aerosols, ~0.6 for ammonium sulfate and nitrate, and ~1 for sodium chloride and sea spray aerosols. The effective hygroscopicity of mixed aerosols can be approximated by a linear combination of the kappa values of the individual chemical components weighted by the volume or mass fractions, respectively [*Andreae and Rosenfeld*, 2008; *Kreidenweis et al.*, 2009; *Pöschl et al.*, 2009]. On average, continental and marine aerosols tend to cluster into relatively narrow ranges of effective hygroscopicity (continental κ = 0.3 ± 0.1; marine κ = 0.7 ± 0.2) [*Andreae and Rosenfeld*, 2008; *Rose et al.*, 2008b].

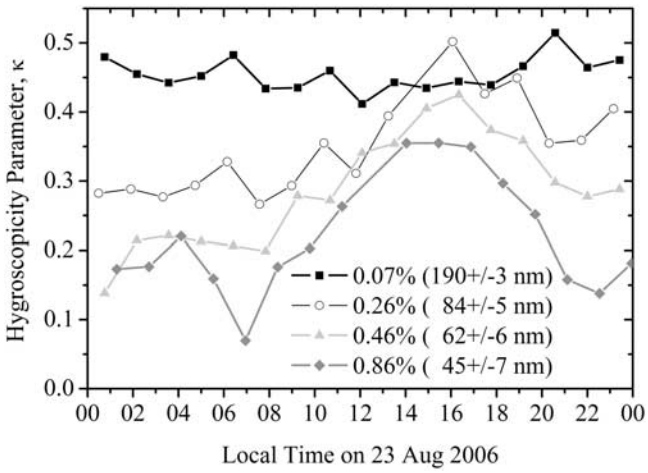

Figure 12. Time series of the hygroscopicity parameter κ measured for selected supersaturations (0.07%, 0.26%, 0.46%, and 0.86%). The values in brackets are the activation diameters measured on average on 23 August 2006 at the respective supersaturations. They indicate the size range for which κ is representative.

[50] At low supersaturation and large diameters (S = 0.07%, ~190 nm), κ remained nearly constant at an average level of ~0.45, which indicates a large proportion of hygroscopic particle components (>50% ammonium sulfate and nitrate). At higher supersaturations corresponding to smaller particle sizes (0.26–0.86%, 40–90 nm), however, κ was much lower in the early morning before the nucleation event (~0.1–0.3), which indicates a large proportion of particle components with low hygroscopicity (≥50% organics and soot). During nucleation and growth, the κ values for the particles in the size range of 40–90 nm increased to a similar level as observed for the ~190 nm particles (~0.35–0.5), but in the evening κ decreased again. Both the rate and the extent of the midday increase and evening decrease of κ were highest for the smallest particles.

[51] The observed changes in the CCN properties are consistent with the AMS measurement data. Around midday and in the early afternoon, the observed increases of κ and N_{CCN} were accompanied by a steep increase of particulate sulfate and a much less pronounced increase of POM. In the late afternoon and evening, however, the increase of POM was much more pronounced, which may be due to enhanced condensation of semivolatile SOA components.

4. Conclusion

[52] The presented case study is typical for new particle formation events in the highly polluted region around Beijing, when clean air is advected or mixed from aloft in the morning after the breakup of the nocturnal inversion layer. The observed evolution of particle number size distribution (banana-shaped contour in time series plot) indicates particle nucleation and growth on a regional scale within one air mass. Owing to concurrent high precursor gas emissions, secondary aerosol mass was produced continuously; the major components were sulfate, ammonium, and organic matter.

[53] Owing to continued high growth rates of particle mass and number mode diameter (~13 μg m^{-3} and 6 nm per hour, respectively), the aerosol nucleation mode grew very quickly into the size range of cloud condensation nuclei. Consequently, the CCN size distribution was dominated by the growing nucleation mode (up to 80% of the total CCN concentration) and not as usual by the accumulation mode, which, to our knowledge, has not been observed before.

[54] For medium and high water vapor supersaturations (0.26–0.86%), the CCN number concentrations increased very rapidly, and only six hours after the nucleation event they reached maximum values of 13,000–19,000 cm^{-3}, which are among the highest CCN number concentrations ever observed. At low supersaturation (0.07%), N_{CCN} exhibited a steady exponential increase from 700 cm^{-3} in the morning to ~4000 cm^{-3} at the end of the day.

[55] For large particles (~190 nm), the effective hygroscopicity parameter κ remained nearly constant at an average level of ~0.45. For smaller particles (40–90 nm), κ was initially much lower (~0.1–0.3); after nucleation and growth it increased to a similar level as observed for the ~190-nm particles (~0.35–0.5), but in the evening it decreased again.

[56] This result is consistent with AMS measurement data of aerosol chemical composition. Around midday and in the early afternoon, the observed increase of κ and N_{CCN} were accompanied by a steep increase of particulate sulfate and a much less pronounced increase of POM. In the late afternoon and evening, the increase of POM was however much more pronounced, which may be due to enhanced condensation of semivolatile SOA components.

[57] **Acknowledgments.** This work as part of CAREBeijing-2006 (Campaigns of Air Quality Research in Beijing 2006) were mainly supported by Beijing Council of Science and Technology (HB200504–6 and HB200504–2). The authors wish to extend their gratitude to all participants for their good humor, enthusiasm, and openness to collaboration in the field measurements at the Yufa site and in the data evaluation. S.S.G., D.R., H.S., and U. P. thank M.O. Andreae and the Max Planck Society for support.

References

Achtert, P., W. Birmili, A. Nowak, B. Wehner, A. Wiedensohler, N. Takegawa, Y. Kondo, Y. Miyazaki, M. Hu, and T. Zhu (2009), Hygroscopic growth of tropospheric particle number size distributions over the North China Plain, *J. Geophys. Res.*, doi:10.1029/2008JD010921, in press.

Andreae, M. O. (2008), Correlation between cloud condensation nuclei concentration and aerosol optical thickness in remote and polluted regions, *Atmos. Chem. Phys. Discuss.*, *8*, 11,293–11,320.

Andreae, M. O., and D. Rosenfeld (2008), Aerosol-cloud-precipitation interactions. Part 1. The nature and sources of cloud-active aerosols, *Earth Sci. Rev.*, *89*, 13–41, doi:10.1016/j.earscirev.2008.03.001.

Birmili, W., F. Stratmann, and A. Wiedensohler (1999), Design of a DMA-based size spectrometer for a large particle size range and stable operation, *J. Aerosol Sci.*, *30*, 549–553, doi:10.1016/S0021-8502(98)00047-0.

Burtscher, H., et al. (2001), Separation of volatile and non-volatile aerosol fractions by thermodesorption: Instrumental development and applications, *J. Aerosol Sci.*, *32*, 427–442, doi:10.1016/S0021-8502(00)00089-6.

Cheng, Y. F., et al. (2009), Influence of soot mixing state on aerosol light absorption and single scattering albedo during air mass aging at a polluted regional site in northeastern China, *J. Geophys. Res.*, doi:10.1029/2008JD010883, in press.

Frank, G. P., U. Dusek, and M. O. Andreae (2006), Technical note: A method for measuring size-resolved CCN in the atmosphere, *Atmos. Chem. Phys. Discuss.*, *6*, 4879–4895.

Frey, A., D. Rose, B. Wehner, T. Müller, Y. Cheng, A. Wiedensohler, and A. Virkkula (2008), Application of the Volatility-TDMA technique to determine the number size distribution and mass concentration of less volatile particles, *Aerosol Sci. Technol.*, *42*, 817–828, doi:10.1080/02786820802339595.

Garland, R. M., et al. (2009), Aerosol optical properties observed during CAREBeijing-2006: Characteristic differences between the inflow and outflow of Beijing city air, *J. Geophys. Res.*, *114*, D00G04, doi:10.1029/2008JD010780.

Jayne, J. T., D. C. Leard, X. Zhang, P. Davidovits, K. A. Smith, C. E. Kolb, and D. R. Worsnop (2000), Development of an aerosol mass spectrometer for size and composition analysis of submicron particles, *Aerosol Sci. Technol.*, *33*, 49–70, doi:10.1080/027868200410840.

Kaiser, D. P. (1998), Analysis of total cloud amount over China, 1951–1994, *Geophys. Res. Lett.*, *25*(19), 3599–3602, doi:10.1029/98GL52784.

Kaiser, D. P. (2000), Decreasing cloudiness over China: An updated analysis examining additional variables, *Geophys. Res. Lett.*, *27*(15), 2193–2196, doi:10.1029/2000GL011358.

Kondo, Y., et al. (2006), Temporal variations of elemental carbon in Tokyo, *J. Geophys. Res.*, *111*, D12205, doi:10.1029/2005JD006257.

Kondo, Y., Y. Miyazaki, N. Takegawa, T. Miyakawa, R. J. Weber, J. L. Jimenez, Q. Zhang, and D. R. Worsnop (2007), Oxygenated and water-soluble organic aerosols in Tokyo, *J. Geophys. Res.*, *112*, D01203, doi:10.1029/2006JD007056.

Kreidenweis, S. M., M. D. Petters, and P. Y. Chuang (2009), Cloud particle precursors, in *Perturbed Clouds in the Climate System: Their Relationship to Energy Balance, Atmospheric Dynamics and Precipitation*, *Strungmann Forum Rep.*, vol. 2, edited by J. Heintzenberg and R. J. Charlson, MIT Press, Cambridge, Mass., in press.

Kuwata, M., Y. Kondo, Y. Miyazaki, Y. Komazaki, J. H. Kim, S. S. Yun, H. Tanimoto, and H. Matsueda (2008), Cloud condensation nu-

clei activity at Jeju Island, Korea in spring 2005, *Atmos. Chem. Phys.*, *8*, 2933–2948.

Lance, S., J. Medina, J. N. Smith, and A. Nenes (2006), Mapping the operation of the DMT Continuous Flow CCN Counter, *Aerosol Sci. Technol.*, *40*, 242–254, doi:10.1080/02786820500543290.

Menon, S., J. Hansen, L. Nazarenko, and Y. Luo (2002), Climate effects of black carbon aerosols in China and India, *Science*, *297*, 2250–2253, doi:10.1126/science.1075159.

Orsini, D. A., A. Wiedensohler, and D. S. Covert (1996), Volatility measurements of atmospheric aerosols in the mid and south Pacific using a Volatility-Tandem-Differential-Mobility-Analyzer, *J. Aerosol Sci.*, *27*, Suppl. 1, S53–S54, doi:10.1016/0021-8502(96)00099-7.

Petters, M. D., and S. M. Kreidenweis (2007), A single parameter representation of hygroscopic growth and cloud condensation nucleus activity, *Atmos. Chem. Phys.*, *7*, 1961–1971.

Philippin, S., A. Wiedensohler, and F. Stratmann (2004), Measurements of non-volatile fractions of pollution aerosols with an eight-tube volatility tandem differential mobility analyzer (VTDMA-8), *J. Aerosol Sci.*, *35*, 185–203, doi:10.1016/j.jaerosci.2003.07.004.

Pöschl, U., D. Rose, and M. O. Andreae (2009), Climatologies of cloud-related aerosols: Part 2: Particle hygroscopicity and cloud condensation nuclei activity, in *Perturbed Clouds in the Climate System: Their Relationship to Energy Balance, Atmospheric Dynamics and Precipitation*, *Strungmann Forum Rep.*, vol. 2, edited by J. Heintzenberg and R. J. Charlson, MIT Press, Cambridge, Mass., in press.

Qian, Y., D. P. Kaiser, L. R. Leung, and M. Xu (2006), More frequent cloud-free sky and less surface solar radiation in China from 1950 to 2000, *Geophys. Res. Lett.*, *33*, L01812, doi:10.1029/2005GL024586.

Roberts, G. C., and A. Nenes (2005), A continuous-flow streamwise thermal-gradient CCN chamber for atmospheric measurements, *Aerosol Sci. Technol.*, *39*, 206–221, doi:10.1080/027868290913988.

Rose, D., B. Wehner, M. Ketzel, C. Engler, J. Voigtländer, T. Tuch, and A. Wiedensohler (2006), Atmospheric number size distributions of soot particles and estimation of emission factors, *Atmos. Chem. Phys.*, *6*, 1021–1031.

Rose, D., S. S. Gunthe, E. Mikhailov, G. P. Frank, U. Dusek, M. O. Andreae, and U. Pöschl (2008a), Calibration and measurement uncertainties of a continuous-flow cloud condensation nuclei counter (DMT-CCNC): CCN activation of ammonium sulfate and sodium chloride aerosol particles in theory and experiment, *Atmos. Chem. Phys.*, *8*, 1153–1179.

Rose, D., A. Nowak, P. Achtert, A. Wiedensohler, M. Hu, M. Shao, L. Zeng, Y. Zhang, M. O. Andreae, and U. Pöschl (2008b), Cloud condensation nuclei in polluted air and biomass burning smoke near the mega-city Guangzhou, China–Part 1: Size-resolved measurements and implications for the modeling of aerosol particle hygroscopicity and CCN activity, *Atmos. Chem. Phys. Discuss.*, *8*, 17,343–17,392.

Smith, M. H., and C. D. O'Dowd (1996), Observations of accumulation mode aerosol composition and soot carbon concentrations by means of a high-temperature volatility technique, *J. Geophys. Res.*, *101*(D14), 19,583–519,591.

Stratmann, F., and A. Wiedensohler (1996), A new data inversion algorithm for DMPS-measurements, *J. Aerosol Sci.*, *27*, Suppl. 1, S339–S340, doi:10.1016/0021-8502(96)00242-X.

Streets, D. G., et al. (2007), Air quality during the 2008 Beijing Olympic Games, *Atmos. Environ.*, *41*, 480–492, doi:10.1016/j.atmosenv.2006.08.046.

Su, H., Y. F. Cheng, P. Cheng, Y. H. Zhang, S. Dong, L. M. Zeng, J. Slanina, M. Shao, and A. Wiedensohler (2008), Observation of nighttime nitrous acid (HONO) formation at a non-urban site during PRIDE-PRD2004 in China, *Atmos. Environ.*, *42*, 6219–6232, doi:10.1016/j.atmosenv.2008.04.006, in press.

Sullivan, A. P., R. J. Weber, A. L. Clements, J. R. Turner, M. S. Bae, and J. J. Schauer (2004), A method for on-line measurement of water-soluble organic carbon in ambient aerosol particles: Results from an urban site, *Geophys. Res. Lett.*, *31*, L13105, doi:10.1029/2004GL019681.

Takegawa, N., Y. Miyazaki, Y. Kondo, Y. Komazaki, T. Miyakwa, J. L. Jimenez, J. T. Jayne, D. R. Worsnop, J. D. Allan, and R. J. Weber (2005), Characterization of an aerodyne aerosol mass spectrometer (AMS): Intercomparison with other aerosol instruments, *Aerosol Sci. Technol.*, *39*, 760–770.

Takegawa, N., et al. (2009a), Variability of submicron aerosol observed at a rural site in Beijing in the summer of 2006, *J. Geophys. Res.*, *114*, D00G05, doi:10.1029/2008JD010857.

Takegawa, N., et al. (2009b), Performance of an aerodyne aerosol mass spectrometer (AMS) during intensive campaigns in China in the summer of 2006, *Aerosol Sci. Technol.*, *43*, 189–204, doi:10.1080/02786820802582251.

Turpin, B. J., and H.-J. Lim (2001), Species contributions to $PM_{2.5}$ mass concentrations: Revisiting common assumptions for estimating organic mass, *Aerosol Sci. Technol.*, *35*, 602–610, doi:10.1080/02786820152051454.

van Pinxteren, D., E. Brüggemann, T. Gnauk, Y. Iinuma, K. Müller, A. Nowak, P. Achtert, A. Wiedensohler, and H. Herrmann (2009), Size- and time-resolved chemical particle characterization during CAREBeijing-2006: Different pollution regimes and diurnal profiles, *J. Geophys. Res.*, doi:10.1029/2008JD010890, in press.

Wehner, B., W. Birmili, F. Ditas, Z. Wu, M. Hu, X. Liu, J. Mao, N. Sugimoto, and A. Wiedensohler (2008), Relationships between submicrometer particulate air pollution and air mass history in Beijing, China, 2004–2006, *Atmos. Chem. Phys.*, *8*, 6155–6168.

Willeke, K., and P. A. Baron (1993), *Aerosol Measurement: Principles, Techniques, and Applications*, Van Nostrand Reinhold, New York.

Wu, Z., M. Hu, S. Liu, B. Wehner, S. Bauer, A. Maßling, A. Wiedensohler, T. Petäjä, M. D. Maso, and M. Kulmala (2007), New particle formation in Beijing, China: Statistical analysis of a 1-year data set, *J. Geophys. Res.*, *112*, D09209, doi:10.1029/2006JD007406.

Wu, Z., M. Hu, P. Lin, S. Liu, B. Wehner, and A. Wiedensohler (2008), Particle number size distribution in the urban atmosphere of Beijing, China, *Atmos. Environ.*, *42*, 7967–7980, doi:10.1016/j.atmosenv.2008.06.022.

Xu, Q. (2001), Abrupt change of the mid-summer climate in central east China by the influence of atmospheric pollution, *Atmos. Environ.*, *35*, 5029–5040, doi:10.1016/S1352-2310(01)00315-6.

P. Achtert, M. Berghof, W. Birmili, Y. F. Cheng, A. Nowak, B. Wehner, A. Wiedensohler, and Z. J. Wu, Leibniz Institute for Tropospheric Research, Permoser Strasse 15, D-04318 Leipzig, Germany. (achtert@tropos.de; berghof@tropos.de; birmili@tropos.de; cheng@tropos.de; nowak@tropos.de; birgit@tropos.de; ali@tropos.de; zhijunwu@tropos.de)

S. S. Gunthe, U. Pöschl, D. Rose, and H. Su, Biogeochemistry Department, Max Planck Institute for Chemistry, J.J.-Becherweg 27/29, D-55128 Mainz, Germany. (gunthe@mpch-mainz.mgp.de; poeschl@mpch-mainz.mpg.de; rose@mpch-mainz.mpg.de; hsu@mpch-mainz.mpg.de)

A. Hofzumahaus, F. Holland, and A. Wahner, ICG-II, Forschungszentrum Jülich, Leo-Brandt-Strasse, D-52428 Jülich, Germany. (f.hofzumahaus@fz-juelich.de; f.holland@fz-juelich.de; a.wahner@fz-juelich.de)

M. Hu and T. Zhu, State Key Joint Laboratory of Environmental Simulation and Pollution Control, College of Environmental Sciences and Engineering, Peking University, 100871 Beijing, China. (minhucespku@yahoo.com.cn; tzhu@pku.edu.cn)

K. Kita, Y. Kondo, and N. Takegawa, RCAST, University of Tokyo, Tokyo 153 8904, Japan. (kita@atmos.rcast.u-tokyo.ac.jp; y.kondo@atmos.rcast.u-tokyo.ac.jp; takegawa@atmos.rcast.u-tokyo.ac.jp)

S. R. Lou, School of Environmental Science and Technology, Shanghai Jiaotong University, 200052 Shanghai, China. (s.lou@fz-juelich.de)